Mesoporous $LaMnO_{3+\delta}$ perovskite from spray−pyrolysis with superior performance for oxygen reduction reaction and Zn−air battery

Long Kuai[a,b], Erjie Kan[a,b], Wei Cao[c], Marko Huttula[c], Sami Ollikkala[d], Taru Ahopelto[d], Ari-Pekka Honkanen[d], Simo Huotari[d], Wenhai Wang[a], and Baoyou Geng[a,*]

[a] College of Chemistry and Materials Science, The Key Laboratory of Functional Molecular Solids, Ministry of Education, Anhui Laboratory of Molecular-Based Materials, Center for Nano Science and Technology, Anhui Normal University. No.1 Beijing East Road, Wuhu, 241000, P. R. China.

[b] School of Biological and Chemical Engineering, Anhui Polytechnic University, Middle Beijing Road, Wuhu, 241000, P. R. China.

[c] Nano and Molecular Systems Research Unit, University of Oulu, P.O. Box 3000, FIN-90014 Oulu, Finland.

[d] Department of Physics, University of Helsinki, PO Box 64, FI-00014 Helsinki, Finland.

* The corresponding author.

E-mail: bygeng@mail.ahnu.edu.cn

Abstract

Oxygen reduction reaction (ORR) is the key reaction to the efficiency of various electrochemical energy devices. This work reported a non-precious mesoporous $LaMnO_{3+\delta}$perovskite for ORR with remarkable activity by a facile aerosol-spray assisted approach. The mesoporous $LaMnO_{3+\delta}$ shows 3.1 times' activity (at 0.9 V *vs.* RHE) of $LaMnO_3$ obtained from co-precipitation method (LMO-CP). Confirmed by XANES, XPS and BET characterizations, the surface Mn state and high surface area is the source to the notably enhanced activity. The study of Zn-air batteries device further confirmed that the Pt/C comparable performance in the practical devices of the obtained mesoporous $LaMnO_{3+\delta}$ catalyst, where the power density at 200 mA/cm^2 is only 2.1% lower than the battery with same-loaded Pt/C catalyst. Therefore, the high mass activity and low-cost of Mn/La may make $LaMnO_{3+\delta}$ further approach to the application of electrochemical devices.

Keywords: $LaMnO_{3+\delta}$; mesoporous; oxidation state; oxygen reduction reaction; Zn-air battery

1. Introduction

Driven by the increasing environment and energy problems, people have been interested in the sustainable and green power sources[1,2]. Due to the environment-friendly power generation form and high energy/power density, the electrochemical energy devices, such as polymer electrolyte membrane fuel cells and rechargeable metal-air batteries, have attracted the widespread attention of scientists[3,4]. Oxygen reduction reaction (ORR), the cathodic process of electrochemical energy cells, determines the overall device performance due to its sluggish 4e pathway and high reaction barriers[5-7]. In general, the precious Pt group (PG) catalysts are demanded to obtain high ORR kinetics[8,9]. Limited by their high-cost and ultra-low earth-abundance, the scientists are therefore trying best to search cheap catalysts with performance approaching to PG catalysts, and many excellent candidates have been investigated. Typically, heteroatom-doped carbon nanomaterials[10-14], metal oxides/N-rGO hybrids[15-17], transition metal carbide/heteroatom-doped carbon[18,19], and perovskites[20-27] have been extensively studied during the recent years.

Among the non-Pt group (NPG) catalysts, perovskites (ABO_3) with high conductivity have been paid extra-attention since they were found to possess excellent intrinsic activity for oxygencatalysis[22,28], typically for $LaMnO_{3+\delta}$ that has the currently most comparable intrinsic activity to the commercial Pt/C catalyst. It is well known that the appratent ORR activity of $LaMnO_{3+\delta}$ is highly sensitive to the preparation method relative to both the state of Mn and specific surface area[26-28].

For example, the conventional solid-state reaction with high reaction temperature always leads to the particles' size as large as hundreds of nanometers[28-32], which displays a inferior appratent activity less than 1.0 A/g (at 0.9 V *vs.* RHE) although the materials have a high intristine activity. Besides, other routes like co-precipitation method has been developed to efficiently prepare perovskite nanoparticles with surface area of 5~30 m^2/g[33,34], unfortunately, the products are mainly lower-active phase and the appratent activity also presents low level. Acturally, the appratent activity of $LaMnO_{3+\delta}$ catalysts is still far from the commercial Pt/C level. Therefore, it is still desirable to prepare nanosized $LaMnO_{3+\delta}$ with preferred phase for high efficiency ORR.

In this work, we presented a mesoporous $LaMnO_{3+\delta}$ catalyst with commercial Pt/C comparable performance by an efficient nitrate spray-pyrolysis method (NSPM). The as-obtained meoporous $LaMnO_{3+\delta}$ shows a preferred rhombohedral phase with dominant surface Mn^{4+} and high specific surface area of 24.8 m^2/g, which contributes 3.1 timesactivity ofthe $LaMnO_3$nanoparticles prepared by co-precipitation (LMO-CP). The study of Zn-air batteries device further confirmed that the Pt/C comparable performance in the practical devices of the mesoporous $LaMnO_{3+\delta}$ catalyst. Therefore, as an excellent NPG catalysts for ORR, the high activity and low-cost of Mn/La may make mesoporous $LaMnO_{3+\delta}$ further approach to the application to the electrochemical devices.

2. Experimental Section

2.1 Chemicals and Materials

All the chemicals are analytical grade, and used as received without further purification. The metal salts, NaOH (AR), and KOH (99.99%) were bought from Aladdin. The triblock polymer Pluronic P-123 ($EO_{20}PO_{70}EO_{20}$) was purchased from Sigma. The Pt/C catalyst (20% Pt loading) and Nafion (5 wt.%) solution was obtained from Dupont Co. Ltd. The water used in this study is with resistance more than 18 MΩ.

2.2 Synthesis of Porous $LaMnO_{3+\delta}$ Microspheres

The devices and method is similar to our previous work. Typically, 1 mmol$Mn(NO_3)_2$, 1 mmol $La(NO_3)_3$ and 0.25 g P123 was dissolved in 20 mL ethanol. The solution was sprayed by a household ultrasonic humidifier (1.7 MHz, 35 W). The generated mist was drawn into a glass tube in a tube furnace (67 cm, pre-heated to 480 ^oC) by a vacuum pump. The products were collected with a filter paper. The porous products were obtained after calcination in air at 700 ^oC for 4 h at a heating rate of 5 ^oC/min.

The porous $LaNiO_3$, $LaCoO_3$, and $LaCo_{0.8}Fe_{0.2}O_3$ were prepared with the same method except the calcination temperature is 600 ^oC. For the synthesis of $LaNiO_3$, the calcination is under O_2 (purity > 99.4%) flow. $La_{0.5}Sr_{0.5}CoO_{3-\delta}$ and $La_{0.5}Sr_{0.5}Co_{0.8}Fe_{0.2}O_3$ are obtained by calcination at 800 ^oC.

2.3 Synthesis of $LaMnO_3$ Nanoparticles (LMO-CP)

The $LaMnO_3$ nanoparticles are prepared by a co-precipitation method. [34] 1 mmol$Mn(NO_3)_2$ and 1 mmol $La(NO_3)_3$ were dissolved in 10 mL water. 3 mL of 1.7 M NaOH solution was subsequently added. The precipitation was washed, collected, dried and finally calcined at 700 ^oC for 8 h in air with a heating rate of 5 ^oC/min.

2.4 Characterizations

The samples were characterized by X-ray diffraction (XRD; Philips X'Pert with Cu $K_{\alpha 1}$ radiation (λ=0.154056 nm)), scanning electron microscopy (SEM; Hitachi S–4800) with 5 kV accelerating voltage, transmission electron microscopy (TEM) and high–resolution TEM (HRTEM) (Tecnai G2 20 S–TWIN) with 200 kV accelerating voltage. The elements' EDX mapping was performed by SEM (Hitachi S–5500) with 30 kV accelerating voltage. X–ray photoelectron spectroscopy (XPS) experiments were conducted on ESCALAB 250 (America) at 15 kV. The Brunauer–Emmett–Teller (BET) specific surface areas and Barrett–Joyner–Halenda (BJH) pore size distributions were measured and analyzed by N_2sorption isotherms (77 K) with 3Flex Surface Characterization Analyzer (Micromeritics, America).

X-ray Absorption Measurements: The XANES measurements were performed on a home-laboratory spectrometer based on a spherically bent Si(440) and Si(531) monochromator crystals in the Johann geometry, curvature radius 500 mm.[52] The design is similar to that of Seidler et. al.[53, 54] The x-ray tube with an Ag-anode was operated at 20 kV voltage and 2 mA current as the incident photon source. The monochromated x-rays were focused on a powder sample in front of a NaI scintillator detector. The detector and monochomator followed the Rowland circle with linear translation motors and a goniometer for the selection of the Bragg angle.

Electrode Preparation and ORR Measurements: The glassy carbon electrode (5 mm in diameter, Pine Instrument) was polished with 1 and 0.05 μm Al_2O_3 powder in order. The catalyst ink was prepared by mixing 5 mg catalyst powder, 1 mg carbon

(Vucan XC-72, Carbot), 10 μL of 5 wt.% Nafion (Dupont), 0.66 mL H_2O and 0.34 mL dimethylfomamide (DMF) with assistance of ultrasonic treatment for 5 minutes. 10 μL of the catalytic ink was dropped onto the polished glassy carbon electrode and dried naturally. The catalyst loading was 0.25 mg cm^{-2}. For the carbon black modified electrodes, the mass loading was 0.05 mg cm^{-2}. The electrodes with catalyst loadings of 0.125 and 0.05 mg cm^{-2} were prepared by reducing the amount of active materials.

The ORR measurements were performed in 0.1 M KOH solution by a three-electrode system with an electrochemistry workstation (CHI 660C), where the Ag/AgCl electrode (KCl saturated) was used as reference electrode, and Pt plate (1 cm*1 cm*0.02 cm) was used as counter electrode. The static cyclic voltammograms (CVs) were recorded under N_2 (purity > 99.999%) and O_2 (purity > 99.999%) saturated 150 mL of 0.1 M KOH, respectively.The rotating disk (glassy carbon) electrode measurements were performed at the rotating speeds of 400, 625, 900, 1225 and 1600 rpm (Pine Instrument rotator).The rotating ring (Pt)-disk (glassy carbon) electrode (RRDE, 37% collection efficiency, Pine) measurements were performed at the rotating speed of 1600 rpm, and the potential of ring electrode was set at 0.2 V (*vs.* Ag/AgCl electrode). The current-time curves were recorded at -0.5 V (vs. Ag/AgCl electrode) at a RDE rotating rate of 1225 rpm. All the scanning rates were 10 mV/s.

The potential was iR-corrected and referenced to reversible hydrogen electrode (RHE), which was calibrated with the peak position of Mn sites in the literature. Consequently, $E_{RHE} = E_{applied} + 0.960 - iR$, where $E_{applied}$ is the applied potential *vs.*Ag/AgCl electrode and R stands for the Ohm resistance (~43 Ω in this work). In

this work, dual references (Ag/AgCl and RHE) to potential are presented to facilely cross-compare the result with literatures, and all the potentials in the results discussion are referenced to RHE except for special description.

*Zn-Air Battery Assembly and Test:*A home-built Zn-air battery was assembly with a Zn plate with diameter of 1.5 cm as anode, a catalyst-modified gas diffusion electrode (GDE, PTFE-treated hydrophobic carbon paper) with active area of about 1.0 cm^2 as cathode, and a filter paper as separator. About 0.3 mL of 6.0 M KOH solution was added into the cell as the electrolyte. A metal net was covered on the GDE as the cathode current collector. The loading of active materials in GDEs for all the batteries was about 2 mg/cm^2. For the oxide catalysts, 0.5 mg/cm^2 of carbon black (Vucan XC-72, Carbot) was added to increase the conductivity. The resistance of the cell was about 0.8 Ω. The cell measurements were performed under the O_2 flow with the temperature of about 20 ^oC.

3. Results and Discussion

3.1 Synthesis and Characterizations

The synthesis procedure of mesoporous $LaMnO_{3+\delta}$ microspheres consists of amorphous precursor preparation and subsequent calcination process. Firstly, the amorphous $LaMnO_3$ precursor was prepared by NSPM as reported in our previous work [35,36]. As illustrated in **Fig. 1a**, the NSPM process consists of spraying the mother solution (part i, containing $Mn(NO_3)_2$, $La(NO_3)_3$ and Pluronic P-123 ($EO_{20}PO_{70}EO_{20}$)), pyrolysis of nitrates (part ii), and powder collection (part iii). Finally, the mesoporous $LaMnO_{3+\delta}$ microspheres are obtained by thermal treatment.

As shown in the scanning electron microscopy (SEM) image (**Fig. 1b**), the amorphous $LaMnO_3$ microspheres with sizes of 0.886±0.300 μm are solid and surface-smooth. After calcination for removal of P-123 template, the obtained $LaMnO_{3+\delta}$ products exhibit typical porous structures with sizes of 0.716±0.310 μm (**Fig. 1c**). The transmission electron microscopy (TEM) image (**Fig. 1d**) further presents the detailed porous structure information. The microspheres are assembled by nanoparticles with sizes of 35−60 nm. The pore sizeis ranged from 20 to 50 nm. Based on the N_2adsorption-desorption isotherm measurement (**Fig. S1a**), the mesoporous $LaMnO_{3+\delta}$ products have a high Brunauer–Emmett–Teller (BET) specific surface area of 24.8 m^2/g and Barrett-Joyner-Halenda (BJH) pore size centered at ~30 nm (**Fig.S1b**), favorable for catalytic active site exposure. Successively, the high-resolution TEM (HRTEM) image (**Fig. 1e**) shows the lattice spacing of 0.29 nm, which can be indexed to the {110} plane. Moreover, the energy-dispersive X-ray (EDX) elemental mapping (**Fig. 1f**)confirms the presence of O, Mn and La elements. Importantly, the O (green), Mn (white) and La (red) elements are found to be well overlapped with each other, suggesting the uniform distribution of Mn and La in $LaMnO_{3+\delta}$. In addition, some other mesoporous perovskite oxides were also prepared by NSPM in this work for meaningful comparison, such as $LaCoO_3$ (LCO), $LaNiO_3$ (LNO), $La_{0.5}Sr_{0.5}CoO_{3-\delta}$ (LSCO), *etc*. (**Fig. S2**)

X-ray powder diffraction (XRD) patterns were performed to analyze the crystalline phase of products. As show in **Fig. 2a**, only perovskite phase (black) with low crystallization degree was observed when $LaMnO_3$ precursor was calcined at 600 ^oC

for 4 h. When the temperature was increased to 700 ^{o}C, the well-crystallized $LaMnO_{3+\delta}$ products were obtained (blue). It is interesting that the obtained sample is rhombohedral phase (green, JCPDS NO. 50-299), which is the preferred phase for ORR [27]. Several diffraction peaks split into two peaks (the dashed box) and one weak peak centered at 2θ of 38.5^{o} appears (insets). For meaningful comparison, we also prepared the $LaMnO_3$ nanoparticles by co-precipitation (marked as LMO-CP)[34]. The obtained LMO-CP possesses particle sizes 40−70 nm (**Fig. S3a, b**) and BET specific surface area of 16.4 m^2/g (**Fig. S3c**). Different from the mesoporous $LaMnO_{3+\delta}$ from NSPM, the LMO-CP presents cubic phase (red), and neither peak centered at 2θ of about 38.5^{o} nor obvious peak splitting can be observed through its XRD pattern. The XRD patterns of other products obtained from NSPM are also confirmed to be perovskite structure (**Fig.S4**) after calcination.

The Mn K-edge x-ray absorption near edge structures (XANES) were investigated to figure out the difference in the synthetic samples. The XANES spectra of the mesoporous $LaMnO_{3+\delta}$ (blue) and LMO-CP (red) were depicted in **Fig. 2b** along with these from the MnO (black), Mn_3O_4 (green), and MnO_2 (orange) for comparison purposes. In general, the X-ray absorption spectrum (XAS) of the $LaMnO_{3+\delta}$ resembles the one of the $LaMnO_3$, with clear features of the pre-edge bump at ~6540 eV, white line at 6557 eV, and a post-edge bump at 6568 eV. The white line positions of the two samples stay between these of MnO and Mn_3O_4, but much lower in energy than the one from MnO_2, which is consistent to the perovskite phase. No obvious energy shift was found between the samples, indicating the similar Mn oxidation state

in the bulk. However, obvious differences are seen at the width of the white line and the height of the pre-edge pumps. Narrowing the main peak refers to the asymmetrisation of the Mn 4p orbital caused by the rhombohedral phase in the $LaMnO_{3+\delta}$ rather than the cubic phased matrix, in line with previously reported first-principles evaluations on similar systems [37]. Interestingly, the signature of the e_g states and its changes can be identified in the K-edge XANES. In the inset of Fig. 2b, clear changes of the pre-edge 'bump' intensity can be seen. This 'bump' bears the hybridizations of the 4p orbitals to the 3d orbitals of the Mn neighboring atoms, yet populating the 3d partial density of states, and associating to the transition to the e_g states [38]. Compared with the LMO-CP, slight decrease of the pump intensity is found in the $LaMnO_{3+\delta}$, indicating the higher e_g occupy. The $LaMnO_{3+\delta}$ exhibit much higher activity than that of LMO-CP, which dissatisfies the result on e_g electron indicator. Thus, the state of surface Mn may play more dominant role in the ORR process, which would be discussed later.

X-ray photoelectron spectra (XPS, **Fig. 2c**,**d** and **S5**) were performed to confirm and compare the surface chemical environment of the as-prepared $LaMnO_{3+\delta}$ and LMO-CP samples. As shown in the left of **Fig. 2c**, the binding energy (E_b) peak of Mn2p in rhombohedral $LaMnO_{3+\delta}$ (642.13 eV) is positively shifted by 0.44 eV compared with LMO-CP (641.69 eV), indicating the higher surface oxidation state of Mn in $LaMnO_{3+\delta}$, which is different from that in the bulk determined by XANES. This is not surprising since the effective detection depth of the XPS allows only surface state probations while the tender X-ray penetrates the powders. The surface

oxygen spectra (right of **Fig. 2c**) further reveals this claiming. The peaks centered at the lower E_b^{O1s} are assigned to the lattice O and the ones centered at the higher E_b^{O1s} are corresponded to –OH [39]. Firstly, there is only a slight E_b^{O1s} difference (0.08 eV) of -OH because the Pauling's electronegativity of H (2.20) is much larger than the electronegativity difference of Mn between $LaMnO_{3+\delta}$ and LMO-CP. While, the E_b^{O1s} peak for lattice O of $LaMnO_{3+\delta}$ (529.50 eV) is positively shifted by extraordinary 0.52 eV than that of LMO-CP (528.98 eV).Moreover, the E_b^{O1s} peak for lattice O of $LaMnO_{3+\delta}$ falls in the region between the E_b peak in $LaMnO_3$ (~529 eV) [40] and MnO_2 (530 eV) [39]. Successively, we made an assignment of the peaks for various oxidation states of surface Mn by fitting the Mn2p spectra (**Fig. 2d** and **Table S1**). Resultantly, the $LaMnO_{3+\delta}$possesses more proportion of Mn^{IV} (43.4%, left of **Fig. 2d**) than LMO-CP (31.0%, right of **Fig. 2d**). Besides, consistent with the previous reports[41], the surface segregation of La_2O_3 was also found in two products that XPS shown that the surface Mn/La ratio is 0.54 and 0.78 in $LaMnO_{3+\delta}$ and LMO-CP, respectively. The larger La_2O_3 segregation in rhombohedral $LaMnO_{3+\delta}$ surface may be responsible for the larger surface Mn^{4+} proportion.

3.2 Electrocatalytic Performance toward ORR in Alkaline Media

The electrocatalytic activity of the mesoporous $LaMnO_{3+\delta}$ and LMO-CP toward ORR was evaluated in an O_2-saturated 0.1 M KOH solution. The carbon black and commercial Pt/C catalysts with identical electrochemical active surface area of 46.0 m^2/g (**Fig. S6**) were also investigated for meaningful comparison. Besides, several repeated measurements with graphite rod instead of Pt plate as counter electrode were

also performed to exclude the possible effect of counter electrode on the results (**Fig. S7**). As displayed in **Fig. 3a**, obvious O_2 reduction peaks are found for all these samples. As presented in **Table 1**, the ORR peak for $LaMnO_{3+\delta}$ (red) is centered at 0.872 V with peak current density (j_p) of 0.75 mA/cm^2, which is 27 mV higher than LMO-CP (pink, 0.845 V with j_p of 0.57 mA/cm^2). Furthermore, the activity of $LaMnO_{3+\delta}$ is even comparable to the same mass-loaded commercial Pt/C catalyst, whose peak potential is just 25 mV lower than that of Pt/C (green, 0.897 V). Successively, the ORR polarization curves on rotating disk electrode (RDE) (Figure 3b) were recorded at a rotating speed of 1600 rpm. Herein, all the ORR polarization curves have been corrected by removing the background currents that measured under the N_2-saturated electrolyte. We also present the ORR polarization of carbon black, which suggests that the activity of carbon black (blue) used in catalyst ink can be negligible for discussing the activity of oxides. Apart from the carbon black, all the limiting current densities (j_L) of porous $LaMnO_{3+\delta}$ (red), LMO-CP (pink) and Pt/C catalysts (green) are highly close to the theoretical j_L (5.75 mA/cm^2 at 1600 rpm), indicating a near 4e ORR pathway. While, the half-wave potential ($E_{1/2}$) for the porous $LaMnO_{3+\delta}$ ($E_{1/2}$ = 0.852 V) is 50 mV positive than LMO-CP ($E_{1/2}$ = 0.802 V). Moreover, the activity of porous $LaMnO_{3+\delta}$ is highly approaching to that of the same-loaded commercial Pt/C catalyst: The $E_{1/2}$ for the porous $LaMnO_{3+\delta}$ is just 36 mV lower than Pt/C, further indicating a superior ORR catalytic activity of $LaMnO_{3+\delta}$ with relatively low cost. Besides, we also studied the ORR electrocatalytic

performance of the as-prepared porous $LaNiO_3$ and $LaCoO_3$. However, their activity is far worse than that of the $LaMnO_{3+\delta}$ (**Fig. S8**) in the same condition.

The electron transfer number (n), directly associated with the ORR pathway, is used to evaluate the ORR efficiency. The Koutecky-Levich equation [42,43] (Eq. (1) and (2)) is used to estimate the n value.

$$j^{-1} = j_k^{-1} + j_d^{-1} \quad (1)$$

$$j_d = 0.62nFC_0D_0^{2/3}\nu^{-1/6}\omega^{1/2} \quad (2)$$

In the Koutecky-Levich equation, the j is the measured Faradic current density, j_k is the kinetic-limiting current density, j_d is the diffusion-limiting current at the RDE rotating speed of ω (rad/s), n is the transferred electron number, F is the Faraday constant (96485 C), C_0 is the bulk concentration of dissolved O_2 (1.21 mol/m^3 in 0.1 M KOH), D_0 is O_2 diffusion coefficiency (1.87×10^{-9} m/s in 0.1 M KOH), ν is kinematic viscosity of electrolyte (1×10^{-6} m^2/s for 0.1 M KOH) and ω is the angular frequency of RDE rotation. Given the above conditions, there is a linear relationship between j^{-1} and $\omega^{-1/2}$. **Fig. 3c** shows the Koutecky-Levich analysis of the j with different rotation rates of 400, 625, 900, 1225 and 1600 rpm (**Fig. S9**) at 0.5 V. When performing the Koutecky-Levich analysis, the Faradic j was corrected by the removal of background current measured under N_2 atmosphere (the black lines in **Fig. S9**). According to the Koutecky-Levich equation, the slope of j^{-1} function of $\omega^{-1/2}$ is associated with the n value of ORR process. The slopes of mesoporous $LaMnO_{3+\delta}$, LMO-CP and Pt/C catalysts are calculated to be 2.201±0.014, 2.265±0.017 and 2.176±0.024 cm^2 mA^{-1} $s^{-1/2}$. Given the n value for Pt/C is 4, the n values for

$LaMnO_{3+\delta}$ and LMO-CP is 3.95 and 3.84, indicating the 4e pathway for both mesoporous$LaMnO_{3+\delta}$ catalyst and LMO-CP.

To discuss the mass activity and intrinsic activity of mesoporous $LaMnO_{3+\delta}$ and LMO-CP, the electrocatalysis with different catalyst loadings was performed (**Fig. S10**). The following activity was based on the measurements with catalysts loading of 0.05 mg cm^{-2}. Firstly, we discuss the mass activity (j_m), which is critical to the device's performance and decided by both the intrinsic activity and specific surface area. The potential-dependent j_m plots of mesoporous $LaMnO_{3+\delta}$, LMO-CP and Pt/C catalysts are displayed in **Fig. 3d**. The j_m of Pt/C catalyst is normalized by the loading of metallic Pt (2 μg). Herein, we discuss j_m at 0.9 V (*vs.* RHE). Thej_m of mesoporous $LaMnO_{3+\delta}$ (red) reaches extraordinary 2.83±0.20 A/g_{oxide}, which is 3.1 times that of LMO-CP (0.90±0.10 A/g_{oxide}, pink). To the best of our knowledge, the mass activity in this work is notably higher than the reported best values of $LaMnO_{3+\delta}$catalysts [31,44,45], and it is even superior to some carbon-based materials with ultralarge specific surface areas (**Table S2**). Furthermore, it is highly worthy to mention that the j_m of $LaMnO_{3+\delta}$ has reached 4.5% of metallic Pt (63.05±4.45 A/g_{Pt}, green). In general, the O_2 mass transport potential loss can be negligible when the catalyst film thickness is less than 20 μm [46,47]. We assume the 0.4 mg_{Pt}/cm^2 of Pt/C catalyst is used to generate electric power. With the mesoporous $LaMnO_{3+\delta}$, a loading of 8.9 mg_{oxide}/cm^2 is required to obtain the same cathode performance. Considered the density of ~7 g/cm^3 of $LaMnO_{3+\delta}$ and 50% porosity of catalyst film [41], the corresponding catalyst film thickness is ~24 μm, where the O_2 diffusion potential loss almost can be ignored.

Moreover, the much more earth abundance of Mn (950 ppm) and La (32 ppm) than Pt (0.003 ppm) [48] makes mesoporous $LaMnO_{3+\delta}$ to be a potential commercial catalyst.

As for the intrinsic activity, the *j* was normalized by the oxides area based on the BET surface areas. Consequently, the intrinsic activity (at 0.9 V *vs.* RHE) of mesoporous $LaMnO_{3+\delta}$ from NSPM (11.5 $\mu A/cm^2_{oxide}$) is 2.1-fold better than that (5.5 $\mu A/cm^2_{oxide}$) of LMO-CP. We propose that the enhanced intrinsic activity stems from the surface state of Mn, although Shao-Horn *et al.*'s work suggest that the activity peak will appear at the e_g-filling slightly lower than 1 for $LaMnO_{3+\delta}$ according to the "volcano shape" relationship between ORR activity and e_g-filling of ABO_3perovskites[28]. However, the present XANES results show that the e_g-filling of $LaMnO_{3+\delta}$ bulk from NSPM is comparable or even slightly higher than LMO-CP. Thus, the bulk e_g-filling contributes less dominantly compared to the surface state of Mn because the electrocatalysis is more sensitive to the surface chemical environment instead of that in the bulk.

Beyond the activity issue, electrocatalytic stability is also critical factor to evaluate the materials. Herein, the long-time continuous ORR tests were carried out to explore the durability of the mesoporous $LaMnO_{3+\delta}$ and Pt/C catalysts. As displayed in **Fig. 3e**, the mesoporous $LaMnO_{3+\delta}$ (red) exhibits better catalytic endurance than commercial Pt/C (black) catalyst.

3.3RRDE Study and Potential Mechanism Discussion

The rotating ring-disk electrode (RRDE) tests were carried out to further study the ORR process of mesoporous $LaMnO_{3+\delta}$ catalyst. As shown in **Fig. 4a**, compared with

the LSVs in N_2-saturated electrolyte, the ring currents relative to peroxide (HO_2^-) yield were detected for both $LaMnO_{3+\delta}$ (red) and LMO-CP (green) catalysts along with the ORR process in O_2-saturated electrolyte. However, the ring current is about two orders of magnitude lower than the disk current, indicating the high efficiency of ORR. The potential-dependent HO_2^- yields and n values were obtained directly from the RRDE test results based on the Eq. (3) and (4)[16,49].

$$(HO_2^-)\ \% = 200 \times \frac{i_{ring}/N}{i_{disk} + i_{ring}/N} \quad (3)$$

$$n = 4 \times \frac{i_{disk}}{i_{disk} + i_{ring}/N} \quad (4)$$

Where the i_{disk} and i_{ring} are the measured Faradic currents in the corresponding disk and ring electrodes, N is the collection efficiency of ring electrode (0.37), and n is the electron transfer number. As for the calculation of n value and HO_2^- yields, both the ring and disk current are background corrected by taking off the currents measured under N_2 atmosphere. As displayed **Fig. 4b**, we can find that both n values (blue) and HO_2^- yield (pink) plots consist 3 parts. In the first potential region before 0.70 V, for both $LaMnO_{3+\delta}$ and LMO-CP, the n values are ~3.99, but they are all decreased to ~3.95 in the part with potential lower than ~0.6 V. Based on the measured n values and HO_2^- yield, the ORR process on $LaMnO_3$-NSPM and LMO-CP all follows the 4e pathway. As for the decreased n number in the potential lower than 0.7 V, the carbon addition may be responsible. According to Savinova*et al.*'s work [30,31], carbon component plays an important role in the ORR process by accelerating the H_2O_2 formation, leading to the high H_2O_2 yield.

There are two couples of redox pairs in $LaMnO_3$surface [50], namely, Mn^{3+}/Mn^{4+} and Mn^{2+}/Mn^{3+} redox couples. According to the CVs (**Fig. 3a**) of $LaMnO_{3+\delta}$ and LMO-CP under N_2 atmosphere, the conversion of Mn^{4+} to Mn^{3+} appears between 0.75 and 1.0 V, and Mn^{3+} conversion to Mn^{2+} starts at the potential after 0.7 V. The Mn^{4+}/Mn^{3+} conversion peak current of mesoporous $LaMnO_3$ from NSPM is larger than that of LMO-CP, indicating more Mn^{4+} in $LaMnO_{3+\delta}$ surface. Meanwhile, it is at this stage, the potential region of Mn^{4+} reduction, that the activity of $LaMnO_{3+\delta}$ surpasses that of LMO-CP rapidly. Many reports have suggested that the ORR activity of Mn-based perovskites is highly dependent of the surface Mn oxidation state [31, 41, 51]. The mixed Mn^{3+}/Mn^{4+} surface is critical to obtain fast ORR kinetics. In addition, according to the XPS result suggests the $LaMnO_{3+\delta}$ from NSPM possesses more surface Mn^{4+} proportion (43.4%) than that in LMO-CP (31%). Therefore, the notably surface Mn^{4+} is the source to the higher pristine activity, which is well consistent with recent reports [41, 43].

3.4Device Performance of Zn-air Batteries

To evaluate the feasibility and performance in a practical device using the obtained mesoporous$LaMnO_{3+\delta}$ catalyst, we built a Zn-air battery. As shown in **Fig. 5a**, the battery consists of Zn plate as anode, catalyst-modified gas diffusion electrode (GDE) as cathode, and 6.0 M KOH as electrolyte. The active area of electrodeis about 1.0 cm^2. The assembly of Zn-air batteries with commercial Pt/C and LMO-CP catalysts is the same. All the catalyst loading on the GDE for the batteries is 2.0 mg/cm^2. For comparison, the battery with bare carbon paper as the cathode was also investigated.

Fig. 5b presents the I-V (red) and I-P (blue) plots of our batteries. As displayed in Table 1, the open-circuit voltage of cell with mesoporous$LaMnO_{3+\delta}$ catalyst is 1.43 V, which is slightly lower than that of with Pt/C (1.47 V). It is worth to mention that the cell voltages and power densities of the batteries with $LaMnO_{3+\delta}$ catalyst is highly approaching to that of with Pt/C catalyst. Moreover, the difference is still small even the current density is increased to hundreds of milliampere per square centimeter. For example, the power density at 200 mA/cm^2 is 198.6 mW/cm^2, which is only 2.1% lower than the battery with same-loaded Pt/C catalyst (202.8 mW/cm^2). However, considering the practical application, the cost of $LaMnO_{3+\delta}$ catalyst is much lower than commercial Pt/C. As for the battery with LMO-CP catalyst, the open-circuit voltage is only 1.38 V, slightly lower than that with the $LaMnO_{3+\delta}$ catalyst. However, the voltage and power density difference is obviously larger and larger with the increase of current density. This finding is well consistent with ORR polarization study, and supports the conclusion of RRDE study that the Mn^{3+}/Mn^{4+} redox pair is more dominant for $LaMnO_{3+\delta}$. Besides, the performance of the cell with bare carbon paper is negligible in comparison with all the batteries with catalyst-modified cathode. Furthermore, **Fig. 5c** vividly displays the digital photos of "LMO"-shaped pattern assembled by 30 light-emitting diodes (LED, nominal power: ~30 mW), which were powered by two tandem home-made Zn-air batteries with $LaMnO_{3+\delta}$ as catalyst. A bright and continuous green emission was observed when the LEDs were powered on. In a word, the obtained $LaMnO_{3+\delta}$ catalyst can produce high device performance, such as Zn-air batteries.

4. Conclusion

In summary, we present the preparation of device-feasible non-precious mesoporous $LaMnO_{3+\delta}$ catalysts by NSPM with superior ORR activity. Contributed by the abundant surface Mn^{4+}, large specific surface area and mesoporous structure, the obtained mesoporous $LaMnO_{3+\delta}$ displayed is 3.1-fold better than that for the$LaMnO_3$ catalystfrom co-precipitation method. It is a new benchmark for the $LaMnO_3$-based perovskite catalysts for ORR in alkaline media. Moreover, the mass activity reaches 22.5% of commercialPt/C catalyst and correspongding 4.5% of metallic Pt while the earth-abundance of La and Mn is 4~5 orders of magnitude higher. The device study of home-built Zn-air batteries further confirmed the feasibility and Pt/C comparable performance in the practical device using the obtained mesoporous $LaMnO_{3+\delta}$as catalyst. This work demonstrate the feasibility of developing mesoporous $LaMnO_{3+\delta}$ materials as high efficiency ORR electrocatalysts.

Acknowledgements

This work was supported by the National Natural Science Foundation of China (21271009, 21471006), the Natural Science Foundation of Anhui Provincial Education Department (KJ2017A111), the Programs for Science and Technology Development of Anhui Province (1501021019).

W.C. and M. H. acknowledge EU Regional Development Fund and Council of Oulu Region. S.O., T.A., A.-P.H., and S. H. were supported by the Academy of Finland (project 1295696).

Appendix A. Supplementary material

References

[1] M. Armand, J. M. Tarascon, Building better batteries, Nature 451 (2008) 652-657.

[2] J. Jiang, Y. Y. Li, J. P. Liu, X. T. Huang, C. Z. Yuan, X. W. Lou, Recent advances in metal oxide-based electrode architecture design for electrochemical energy storage, Adv. Mater. 24 (2012) 5166-5180.

[3] B. C. H. Steele, A. Heinzel, Materials for fuel-cell technologies, Nature 414 (2001) 345-352.

[4] F. Y. Cheng, J. Chen,Metal-air batteries: from oxygen reduction electrochemistry to cathode catalysts, Chem. Soc. Rev.41 (2012) 2172-2192.

[5] V. R. Stamenkovic, B. Fowler, B. S. Mun, G. F. Wang, P. N. Ross, C. A. Lucas, N. M. Marković, Improved oxygen reduction activity on Pt_3Ni (111) via increased surface site availability, Science 315 (2007) 493-497.

[6] M. K. Debe, Electrocatalyst approaches and challenges for automotive fuel cells, Nature 486 (2012) 43-51.

[7] S. J. Guo, S. Zhang, S. H. Sun, Tuning nanoparticle catalysis for the oxygen reduction reaction, Angew. Chem. Int. Ed.52 (2013) 8526-8544.

[8] Y. H. Bing, H. S.Liu, L.Zhang, D.Ghosh, J. J.Zhang, Nanostructured Pt-alloy electrocatalysts for PEM fuel cell oxygen reduction reaction, Chem. Soc. Rev.39 (2010) 2184-2202.

[9] B. Lim, M. J. Jiang, P. H. C. Camargo, E. C. Cho, J. Tao, X. M. Lu, Y. M. Zhu, Y. N. Xia, Pd-Pt bimetallic nanodendrites with high activity for oxygen reduction, Science 324 (2009) 1302-1305.

[10]K. P. Gong, F. Du, Z. H. Xia, M. Durstock, L. M. Dai, Nitrogen-doped carbon nanotube arrays with high electrocatalytic activity for oxygen reduction, Science 323 (2009) 760-764.

[11]L. M. Dai, Y. H. Xue, L. T. Qu, H.-J. Choi, J. B. Baek, Metal-free catalysts for oxygen reduction reaction, Chem. Rev. 115 (2015) 4823-4892.

[12]Y. Zhao, L. J. Liang, S. Chen, X. Z. Wang, Y. W. Ma, Q. Wu, Y. F. Jiang, W. J. Qian, Z. Hu, Can boron and nitrogen co-doping improve oxygen reduction reaction activity of carbon nanotubes, J. Am. Chem. Soc. 135 (2013) 1201-1204.

[13]L. Lin, Q. Zhu, A.-W. Xu, Noble-metal-free Fe–N/C catalyst for highly efficient oxygen reduction reaction under both alkaline and acidic conditions, J. Am. Chem. Soc. 136 (2014) 11027-11033.

[14]W. Zhang, Z. Y. Wu, H.L.Jiang, S. H. Yu, Nanowire-directed templating synthesis of metal–organic framework nanofibers and their derived porous doped carbon nanofibers for enhanced electrocatalysis, J. Am. Chem. Soc. 136 (2014) 14385-14388.

[15]Y. Y. Liang, Y. G. Li, H. L. Wang, J. G. Zhou, J. Wang, T. Regier, H. J. Dai, Co_3O_4nanocrystals on graphene as a synergistic catalyst for oxygen reduction reaction,Nat. Mater.10 (2011) 780-786.

[16]Y. Y. Liang, H. L. Wang, J. G. Zhou, Y. G. Li, J. Wang, T. Regier, H. J. Dai,Covalent hybrid of spinel manganese-cobalt oxide and graphene as advanced oxygen reduction electrocatalysts, J. Am. Chem. Soc. 134 (2012) 3517-3523.

[17]G. Q. Zhang, B. Y. Xia, X. Wang, X. W. Lou, Strongly coupled $NiCo_2O_4$-rGO hybrid nanosheets as a methanol-tolerant electrocatalyst for the oxygen reduction reaction,Adv. Mater. 26 (2014) 2408-2412.

[18]Z.Y. Wu, X. X. Xu, B.C.Hu, H. W. Liang, Y. Lin, L.F.Chen, S.H. Yu, Iron carbide nanoparticles encapsulated in mesoporous Fe-N-doped carbon nanofibers for efficient electrocatalysis,Angew. Chem. Int. Ed.127 (2015) 8297-8301.

[19]J. Wang, H. H. Wu, D. F. Gao, S. Miao, G. X. Wang, X. H. Bao, High-density iron nanoparticles encapsulated within nitrogen-doped carbon nanoshell as efficient oxygen electrocatalyst for zinc–air battery, Nano Energy 13 (2015) 387-396.

[20]Y. L. Zhao, L. Xu, L. Q. Mai, C. H. Han, Q. Y. An, X. Xu, Y. Liu, Q. J. Zhang, Hierarchical mesoporous perovskite $La_{0.5}Sr_{0.5}CoO_{2.91}$ nanowires with ultrahigh capacity for Li-air batteries, Proc. Nat. Acad. Sci., U. S. A.109 (2012) 19569-19574.

[21]J. J. Xu, D. Xu, Z. L. Wang, H. G.Wang, L. L. Zhang, X. B. Zhang, Synthesis of perovskite-based porous $La_{0.75}Sr_{0.25}$ MnO_3 nanotubes as a highly efficient electrocatalyst for rechargeable lithium-oxygen batteries, Angew. Chem. Int. Ed.52 (2013) 3887-3890.

[22]M. Risch, K. A. Stoerzinger, S. Maruyama, W. T. Hong, I. Takeuchi, Y. Shao-Horn, $La_{0.8}Sr_{0.2}MnO_{3-\delta}$ decorated with $Ba_{0.5}Sr_{0.5}Co_{0.8}Fe_{0.2}O_{3-\delta}$: a bifunctional surface for oxygen electrocatalysis with enhanced stability and activity, J. Am. Chem. Soc.136 (2014) 5229-5232.

[23] W. Zhou, J. Sunarso, Enhancing bi-functional electrocatalytic activity of perovskite by temperature shock: acase study of $LaNiO_{3-\delta}$, J. Phys. Chem. Lett. 4 (2013) 2982-2988.

[24] Z. Chen, A. P. Yu, D. Higgins, H. Li, H. J. Wang, Z. W. Chen, Highly active and durable core-corona structured bifunctional catalyst for rechargeable metal-air battery application, Nano Lett.12 (2012) 1946-1952.

[25] X. P. Han, F. Y. Cheng, T. R. Zhang, J. G. Yang, Y. X. Hu, J. Chen, Hydrogenated uniform Pt clusters supported on porous $CaMnO_3$ as a bifunctional electrocatalyst for enhanced oxygen reduction and evolution, Adv. Mater. 26 (2014) 2047-2051.

[26] X. P. Han, T. R. Zhang, J. Du, F. Y. Cheng, Porous calcium-manganese oxide microspheres for electrocatalytic oxygen reduction with high activity, J. Chen, Chem. Sci.4 (2013) 368-376.

[27] E. Symianakis, D. Malko, E. Ahmad, A. S. Mamede, J. F. Paul, N. Harrison, A. Kucernak, Electrochemical characterization and quantified surface termination obtained by low energy ion scattering and X-ray photoelectron spectroscopy of orthorhombic and rhombohedral $LaMnO_3$ powders, J. Phys. Chem. C119 (2015) 12209-12217.

[28] J. Suntivich, H. A. Gasteiger, N. Yabuuchi, H. Nakanishi, J. B. Goodenough, Y. Shao-Horn,Design principles for oxygen-reduction activity on perovskite oxide catalysts for fuel cells and metal–air batteries,Nat. Chem.3 (2011) 546-550.

[29]J. Suntivich, E. E. Perry, H. A. Gasteiger, Y. Shao-Horn,The influence of the cation on the oxygen reduction and evolution activities of oxide surfaces in alkaline electrolyte,Electrocatal.4 (2013) 49-55.

[30]T. Poux, F. S. Napolskiy, T. Dintzer, G. Kéranguéven, S. Y. Istomin, G. A. Tsirlina, E. V. Antipov, E. R. Savinova, Dual role of carbon in the catalytic layers of perovskite/carbon composites for the electrocatalytic oxygen reduction reaction, Catal. Today189 (2012) 83-92.

[31]G. Kéranguéven, S. Royer, E. Savinova, Synthesis of efficient Vulcan-$LaMnO_3$ perovskite nanocomposite for the oxygen reduction reaction, Electrochem. Commun.50 (2015) 28-31.

[32]M. Kakihana, M. Arima, M. Yoshimura, N. Ikeda, Y. Sugitani, Synthesis of high surface area $LaMnO_{3+d}$ by a polymerizable complex method, J. Alloy. Compd. 283 (1999) 102-105.

[33]T. Nitadori, T. Ichiki, M. Misono, Catalytic properties of perovskite-type mixed oxides (ABO_3) consisting of rare earth and 3d transition metals. The roles of the A-and B-site ions, Bull. Chem. Soc. Jpn.61 (1988) 621-626.

[34]A. Mahmood, M. F. Warsi, M. N. Ashiq, M. Sher, Improvements in electrical and dielectric properties of substituted multiferroic $LaMnO_3$ based nanostructures synthesized by co-precipitation method,Mater. Res. Bull.47 (2012) 4197-4202.

[35]L. Kuai, J. Geng, E. J. Kan, C. Y. Chen, Y. D. Liu, Q. Wang, B. Y. Geng, A reliable aerosol-spray-assisted approach to produce and optimize amorphous metal

oxide catalysts for electrochemical water splitting, Angew. Chem. Int. Ed.126 (2014) 7677-7681.

[36]L. Kuai, J. X. Wang, T. Ming, C. H. Fang, Z. H. Sun, B. Y. Geng, J. F. Wang, Aerosol-spray diverse mesoporous metal oxides from metal nitrates, Sci. Rep.5 (2015) 9923.

[37]T. Okumura, Y. Yamaguchi, H, Kobayashi, X-ray absorption near-edge structures of $LiMn_2O_4$ and $LiNi_{0.5}Mn_{1.5}O_4$ spinel oxides for lithium-ion batteries: the first-principles calculation study, Phys. Chem. Chem. Phys. 18 (2016) 17827-17830.

[38] A. Y. Ramos, N. M. Souza-Neto, H. C. N. Tolentino, O. Bunau, Y. Joly, S. Grenier, J.-P. Itié, A.-M. Flank, P. Lagarde, A. Caneiro, Bandwidth-driven nature of the pressure-induced metal state of $LaMnO_3$, EPL,96 (2011) 36002.

[39]J.G. Wang, Y. Yang, Z.H. Huang, F. Y. Kang, Rational synthesis of MnO_2/conducting polypyrrole@carbon nanofiber triaxial nano-cables for high-performance supercapacitors, J. Mater. Chem.22 (2012) 16943-16949.

[40]E. Arendt, A. Maione, A. Klisinska, O. Sanz, M. Montes, S. Suarez, J. Blanco, P. Ruiz, Structuration of $LaMnO_3$ perovskite catalysts on ceramic and metallic monoliths: Physico-chemical characterization and catalytic activity in methane combustion, Appl. Catal. A: General339 (2008) 1-14.

[41]V. Celorrio, E. Dann, L. Calvillo, D. J. Morgan, S. R. Hall, D. J. Fermin, Oxygen reduction at carbon-supported lanthanides: The role of the B-site, ChemElectroChem3 (2016) 283-291.

[42] A. J. Bard, L. R. Faulkner, Electrochemical Methods: Fundamentals and Applications, New York: wiley, 1980.

[43] W. M. Wang, D. Zheng, C. Du, Z. Q. Zou, X. G. Zhang, B. J. Xia, H. Yang, D. L. Akins, Carbon-supported Pd-Co bimetallic nanoparticles as electrocatalysts for the oxygen reduction reaction, J. Power Sources 167 (2007) 243-249.

[44] K. A. Stoerzinger, M. Risch, B. H. Han, Y. Shao-Horn,Recent insights into manganese oxides in catalyzing oxygen reduction kinetics, ACS Catal. 5 (2015) 6021-6031.

[45] A. S. Ryabova, F. S. Napolskiy, T. Poux, S. Y. Istomin, A. Bonnefont, D. M. Antipin, A. Y. Baranchikov, E. E. Levin, A. M. Abakumov, G. Kéranguéven, E. V. Antipov, G. A. Tsirlina, E. R. Savinova, Rationalizing the influence of the Mn (IV)/Mn (III) red-ox transition on the electrocatalytic activity of manganese oxides in the oxygen reduction reaction, Electrochim. Acta187 (2016) 161-172.

[46] J. Suntivich, H. A. Gasteriger, N. Yabuuchi, Y. Shao-Horn, Electrocatalytic measurement methodology of oxide catalysts using a thin-film rotating disk electrode, J. Electrochem. Soc. 157 (2010) B1263-B1268.

[47] C. L. Spiegel, Designing &Building Fuel Cells, The McGraw–Hill Companies (2007).

[48] P. Patnaik, Handbook of Inorganic Chemicals, The McGraw–Hill Companies (2002).

[49] H. X. Zhang, J. Wang, Y. W. Zhang, W. -L. Xu, W. Xing, D. Xu, Y. F. Zhang, X. B. Zhang, ZIF-8 derived graphene-based nitrogen-doped porous carbon sheets as

highly efficient and durable oxygen reduction electrocatalysts, Angew. Chem. Int. Ed.53 (2014) 14235-14239.

[50]J. T. Mefford, W. G. Hardin, S. Dai, K. P. Johnston, K. J. Stevenson, Anion charge storage through oxygen intercalation in $LaMnO_3$perovskitepseudocapacitor electrodes, Nat. Mater. 13 (2014) 726-732.

[51]K. A. Stoerzinger, W. M. Lü, C. J. Li, Ariando, T. Venkatesan, Y. Shao-Horn, Highly active epitaxial $La_{(1-x)}Sr_xMnO_3$surfaces for the oxygen reduction reaction: Role of charge transfer, J. Phys. Chem. Lett.6 (2015) 1435-1440.

[52]M. Rovezzi, C. Lapras, A. Manceau, P. Glatzel, R. Verbeni,High energy-resolution x-ray spectroscopy at ultra-high dilution with spherically bent crystal analyzers of 0.5 m radius, Rev. Sci. Instrum. 88 (2017) 013108.

[53]G. T. Seidler, D. R. Mortensen, A. J. Remesnik, J. I. Pacold, N. A. Ball,A laboratory-based hard x-ray monochromator for high-resolution x-ray emission spectroscopy and x-ray absorption near edge structure measurements, Rev, Sci. Instrum. 85 (2014) 113906.

[54]D. R. Mortensen, G. T. Seidler, A. S. Ditter, P. Glatzel,Benchtop Nonresonant X-ray Emission Spectroscopy: Coming Soon to Laboratories and XAS Beamlines Near You, J. Phys: Conf. Ser. 712 (2016) 012036.

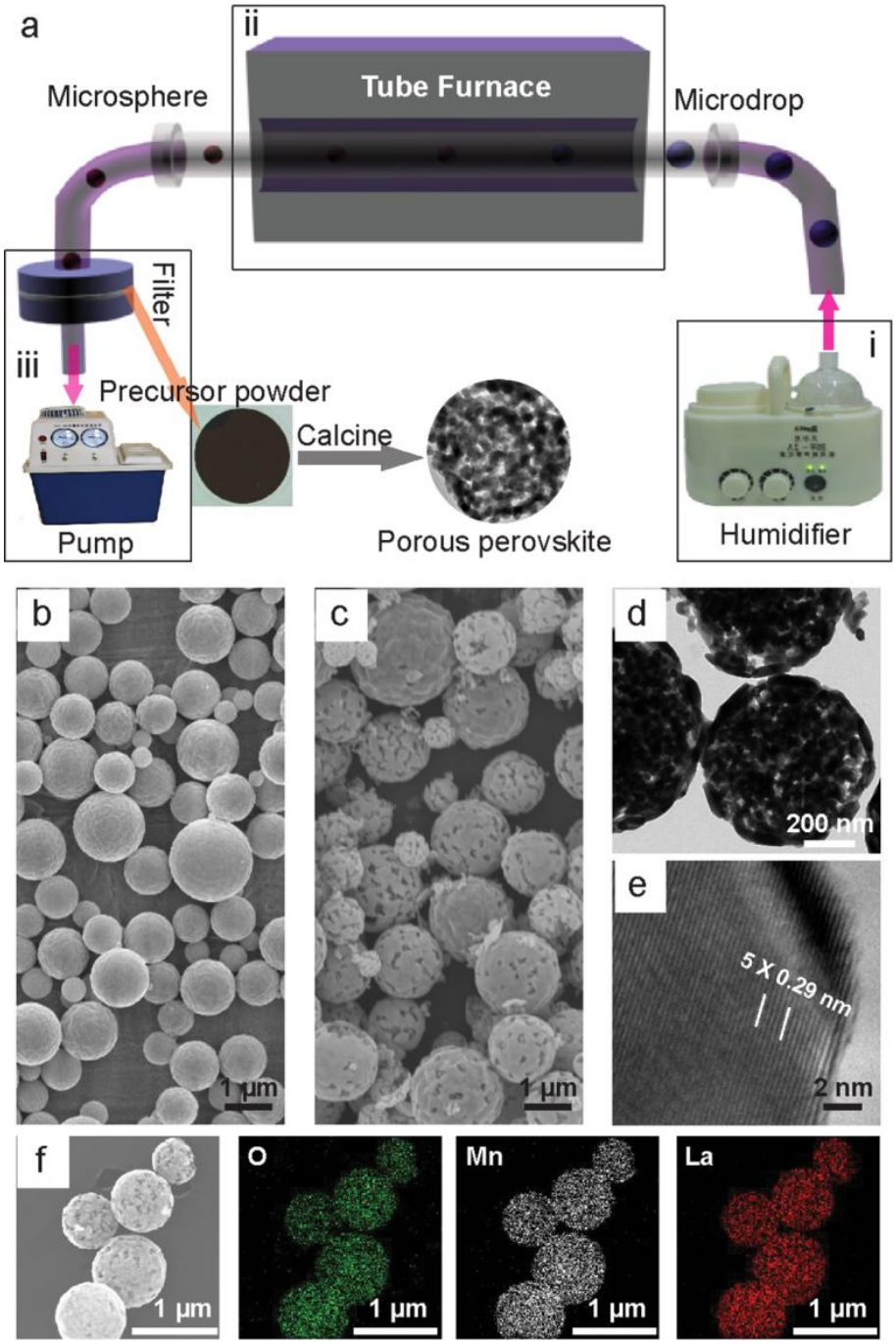

Fig. 1 The synthesis procedure (a) of mesoporous $LaMnO_{3+\delta}$, SEM images of $LaMnO_3$ precursor (b) and mesoporous $LaMnO_{3+\delta}$ product (c), TEM (d), HRTEM (e) images, and EDX-mapping (f) of the mesoporous $LaMnO_{3+\delta}$ microspheres.

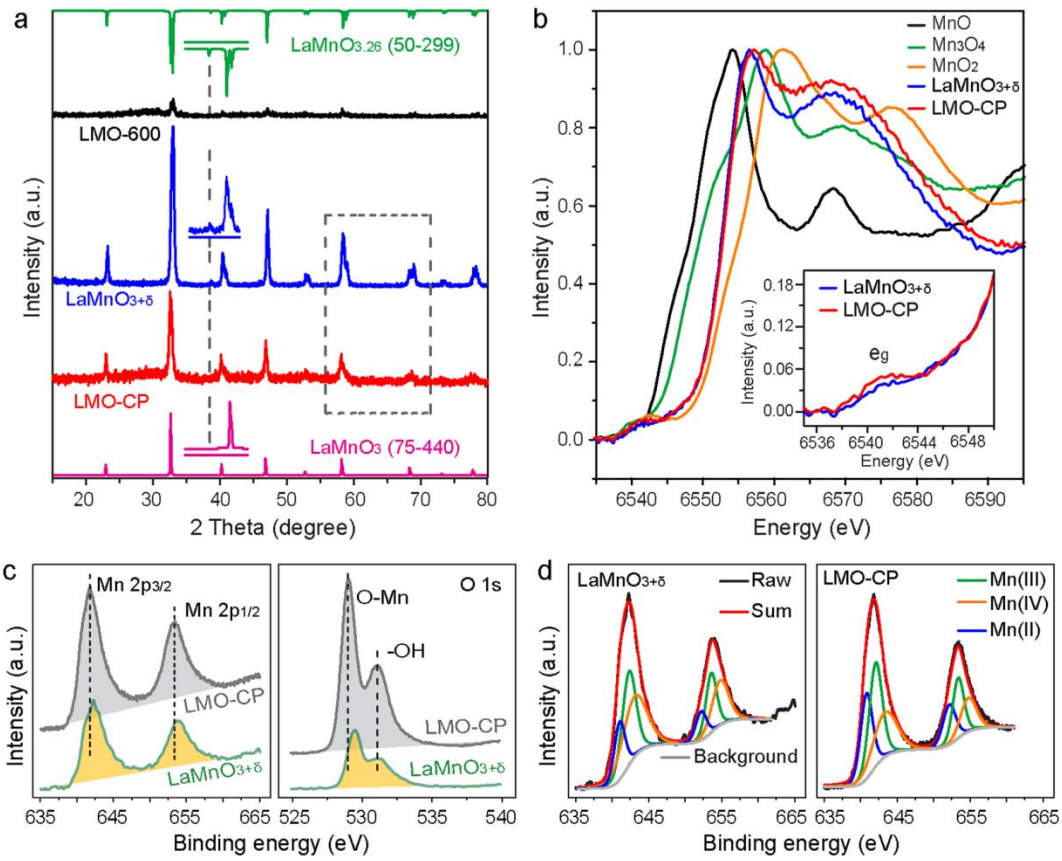

Fig. 2 (a) XRD patterns of LMO-600 (black), mesoporous $LaMnO_{3+\delta}$ (blue), LMO-CP (red) and the standard patterns of rhombohedral $LaMnO_{3.26}$ (blue) and cubic $LaMnO_3$ (pink); (b) Mn K-edge XANES spectra of various samples; (c) XPS Mn2p (left) and O1s (right) spectra of $LaMnO_{3+\delta}$ (gray) and LMO-CP (green); (d) Fitted XPS Mn2p spectra of $LaMnO_{3+\delta}$ (left) and LMO-CP (right).

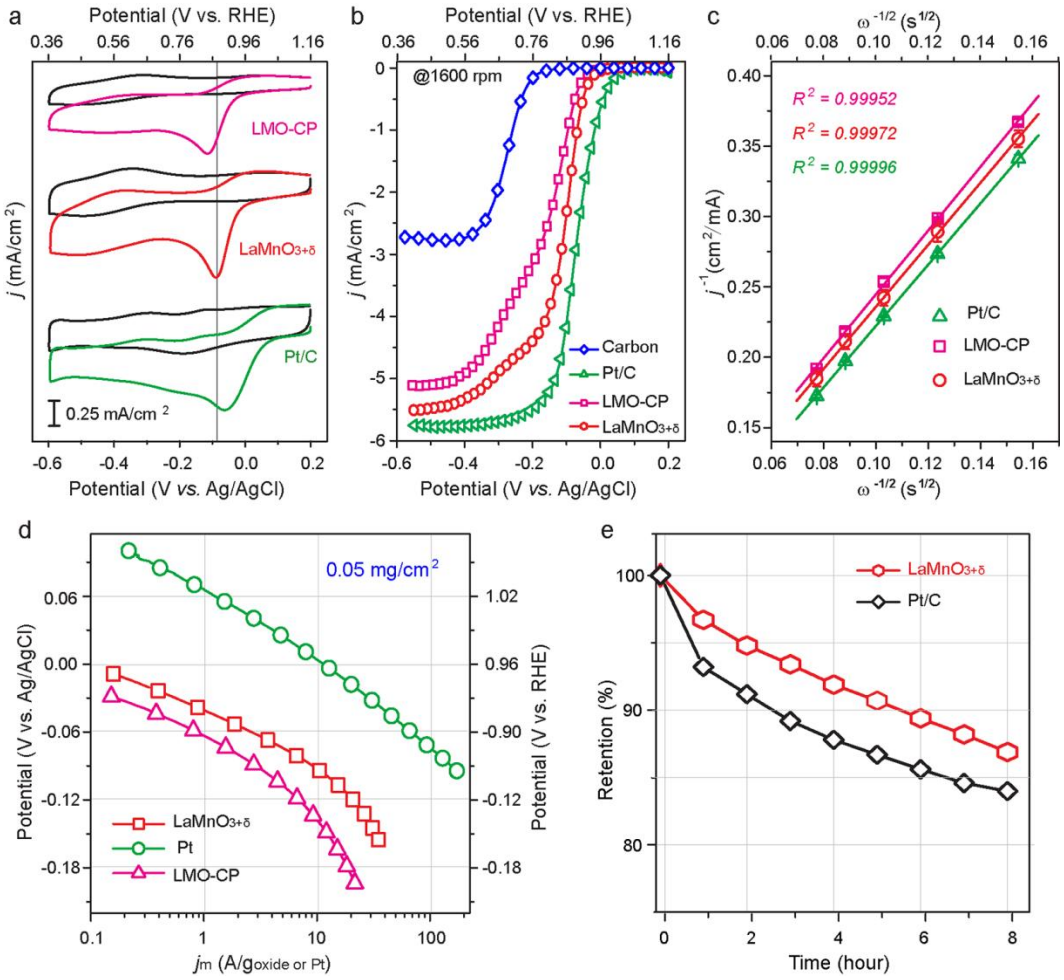

Fig. 3 CVs (a) and LSV curves (b), Koutecky-Levich analysis (c), and potential dependent mass activity plots (d) of mesoporous $LaMnO_{3+\delta}$ (red), LMO-CP (pink) and commercial Pt/C (green) catalysts, and retention plots after long-time electrocatalysis procedure (e) of $LaMnO_{3+\delta}$ (red) and Pt/C (black) catalysts. The error bars in Figure 3c represents the standard deviations of at least 3 independent tests.

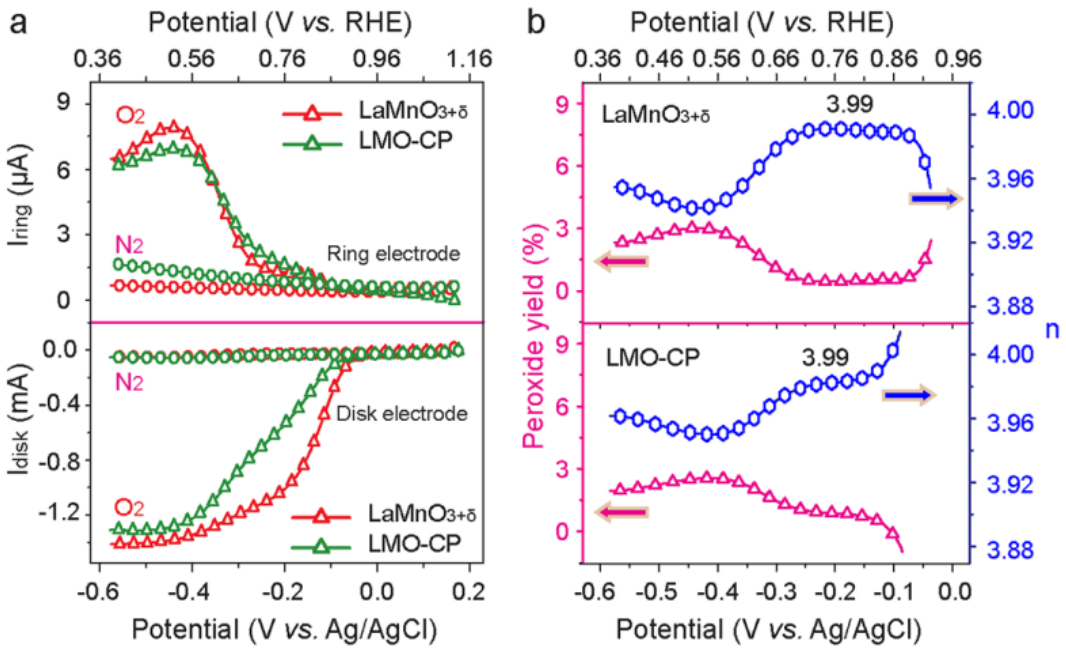

Fig. 4 RRDE tests (a) and potential-dependent peroxide yield (purple) and electron transfer numbers (n) (blue) of mesoporous $LaMnO_{3+\delta}$ and LMO-CP catalyst at the rotation rate of 1600 rpm.

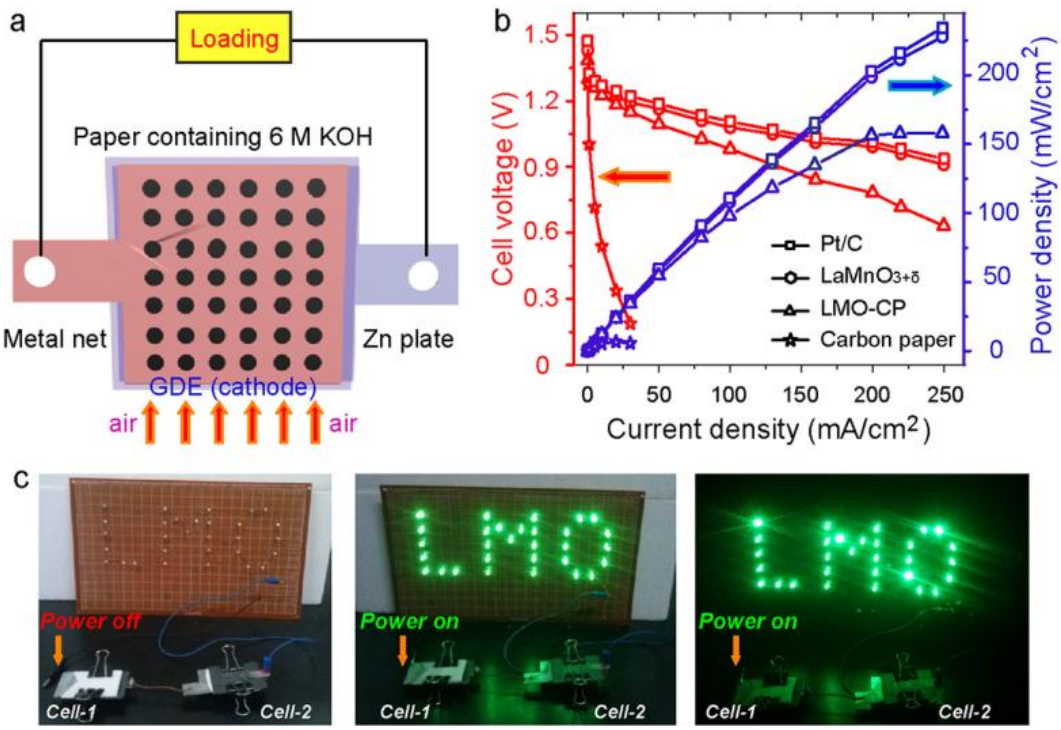

Fig. 5 (a) Scheme of our home-made Zn-air batteries. (b) I-V and I-P plots of Zn-air batteries with bare, mesoporous $LaMnO_{3+\delta}$, LMO-CP and commercial Pt/C catalysts-modified GDE. (c) Digital photos (Left: power-off under daylight; Middle: power-on under daylight; Right: power-on under dark) of "LMO" shaped light-emitting diodes powered by two tandem Zn-air batteries with $LaMnO_{3+\delta}$ as catalyst.

Table 1.A summary of ORR and Zn-air batteries' performance with $LaMnO_{3+\delta}$, LMO-CP and commercial Pt/C catalysts.

Materials	Loading mg/cm^2	E_p V	j_p mA/cm^2	$j_{m,\ 0.9\ V}$[a] A/g	$n_{0.9\ V}$	Voltage of Zn-air batteries V		
						V_{OC}	V 1 mA/cm^2	V 10 mA/cm^2
$LaMnO_{3+\delta}$	0.25	0.872	0.57	2.83±0.20	3.99	1.430	1.322	1.255
LMO-CP	0.25	0.845	0.75	0.90±0.10	3.99	1.384	1.309	1.225
Pt/C	0.25	0.897	0.64	63.05±4.45[b]	4	1.473	1.324	1.271

[a] The mass activity was calculated with catalyst loading of 0.05 mg cm^{-2}.

[b] The j_m was normalized by the loading of metallic Pt (10 μg).

Supporting Information

Click here to download Supporting Information: Supporting Information.docx

***Graphical Abstract**

A device-feasible and Earth-abundant $LaMnO_{3+\delta}$ electrocatalyst is obtained for ORR and Zn-air batteries. Contributed by the surface oxidation state of Mn and high specific surface area, it displayed commercial Pt/C catalyst compared performance.